NIR Laser Integration of Photodetector on 3D Printed Chamber for Colorimetric Biosensing

Ching-fu Lin, Chun-hao Chang, Laurent Noël, Bor-ran Li, Hsin-fei Meng, Olivier Soppera, Hsiao-wen Zan

NIR laser integration of photodetector on 3D printed chamber for colorimetric biosensing

Ching-Fu Lin[1,2,3,4], Chun-Hao Chang[5,6], Laurent Noël[3,4], Bor-Ran Li[5,6,7], Hsin-Fei Meng[8], Olivier Soppera[3,4,*], Hsiao-Wen Zan[1,2,*]

[1]*Department of Photonics and Institute of Electro-Optical Engineering, College of Electrical and Computer Engineering, National Yang Ming Chiao Tung University, Hsinchu, 30010, Taiwan, ROC*

[2]*Department of Photonics and Institute of Electro-Optical Engineering, College of Electrical and Computer Engineering, National Chiao Tung University, Hsinchu, 30010, Taiwan, ROC*

[3]*Université de Haute-Alsace, CNRS, IS2M UMR 7361, F-68100 Mulhouse, France*

[4]*Université de Strasbourg, France*

[5] *Institute of Biomedical Engineering, College of Electrical and Computer Engineering, National Yang Ming Chiao Tung University, Hsinchu, Taiwan*

[6] *Department of Electrical and Computer Engineering, College of Electrical and Computer Engineering, National Yang Ming Chiao Tung University, Hsinchu, Taiwan*

[7]*Center for Emergent Functional Matter Science, National Yang Ming Chiao Tung University, Hsinchu, Taiwan*

[8]*Institute of Physics, National Yang Ming Chiao Tung University, No. 1001, University Road, Hsinchu 300, Taiwan*

Abstract:

In this work, Au NPs (gold nanoparticles)/IZO (indium-zinc-oxide) nanocomposite visible photodetector (PD) was directly prepared by near-infrared (NIR) laser-annealing on a 3D-printed substrate to form an integrated colorimetric sensor. After a surface planarization process, using a low power laser treatment without damaging the substrate, Au NPs were formed from the Au thin layer (6 nm) on 3D-printed resin

substrate by laser assisted dewetting process. Also, the UV-vis photoresponsivity was compared by tuning different NIR laser power intensity for sol-gel IZO curing. By investigating the temperature profile of each laser annealing process and the surface morphology of Au NPs/IZO nanocomposite film, the optimized PD was then integrated with a 3D-printed sensing chamber for successfully demonstrating urea detection varied from 1, 5, 10, 25, 50 mM, which refer to the salivary urea concentrations for healthy and chronic kidney disease groups.

1. Introduction:

Recently, non-invasive, low cost, and compact sensing designs which are associated with Internet of Things (IoT) have attracted much attention in healthcare for human beings, including real-time detection of biosensors for personal health management, environmental quality monitoring, and also the chronic disease tracing **[1-3]**. Among the relative applications, such as heavy metal ions detection **[4]**, toxic gas sensing **[5,6]**, nucleic acid amplification **[7]** and chemical substance check **[8,9]** for human beings, etc, colorimetric sensing has been developed as one of the most useful techniques for demonstrating sensing designs with their convenience of quick detection time, good selectivity and sensitivity, especially for identifying colorimetric samples based on high naked-eye perceptibility **[10,11]**. Besides, UV-vis spectroscopy analysis offered from spectrometers also gives a representative method for quantifying precise colorimetric sensing signals based on Beer-Lambert Law **[12]**. Moreover, in order to promote the portability for extended applications, several works have been proposed for simplifying the designs by combining the specific optical designs with digital images captured by smart phones **[13-18]** for colorimetry analysis **[19]**, or by using optical fibers coated with sensing probes for modulating light

intensity for the photodetector (PD) **[20,21]**. These schemes mainly rely on a system with discrete components, a more integrated and intuitive system to combine the sensing-induced light intensity change and the electrical signal reading is still expected.

Moreover, nowadays the polymer 3D printing technique gradually opens a new direction for fabricating functional and miniaturized bioreactors for colorimetric sensing **[22]**. The 3D-printed microfluidic arrays for nucleic acid amplification tests were developed by K. Kadimisetty et al. **[23]** and K. Yin et al. **[24]**. The mechanical microfluidic device with special torque-actuated pump and valves was designed by H. N. Chan **[25]**, et al. for urine protein detection. The 3D-printed pads with micro channels for leading selective color reaction were presented by H. Baek et al. **[26]** and G. Wang et al. **[27]** for multiple chemical substances detection. Except for image processing-assisted analysis, a 3D-printed flow cell composed with a commercial light-to-voltage sensor and a light source for monitoring the transmission light variation through the flow channel was also demonstrated by Y. Liang et al. **[28]** for nitrite detection, the sensitivity was found to be improved by extending the channel length. Following above works, it is expected that directly fabricating visible-light PDs on the 3D-pinted sensing chamber may provide design flexibility and further facilitate the development of colorimetric sensing technics.

To directly form visible light PDs on a 3D-printed reaction chamber, low temperature process is needed. Organic semiconductor PDs have the advantage of low processing temperature, but usually suffer from the poor lifetime in air. The commonly used glass encapsulation solves the lifetime issue but leads to poor compatibility with the arbitrarily-shaped 3D printed substrate. In order to develop PDs through low cost and low temperature fabrication processes with good operation

stability in air, solution-processed metal oxide (M-O) based photoactive thin films synthesized from metal precursors by sol-gel chemistry are considered. Conventionally, high temperature thermal annealing processes are usually needed for promoting the condensation reaction for forming crosslinked M-O network **[29]**, it is essential to develop technics to lower down the thermal budget **[30]** of functional sol-gel M-O film on resin based substrates. So far, low temperature annealing processes including the adoption of deep-ultraviolet (DUV) light for activating photochemical reaction **[31-35]** or light absorber doping for efficiently extracting heat during NIR laser irradiation **[36]** has been proposed to realize low temperature sol-gel M-O film curing. Particularly, in our prior work, when metal nanoparticles (NPs) coupled with sol-gel M-O film for forming nanocomposite structure, they not only enhanced the photoresponse to visible light due to localized surface plasmon resonance (LSPR) absorption **[37]**, but also worked sufficiently as nanoheaters based on thermoplasmonic effect during NIR laser annealing for sol-gel M-O film curing **[38]**. Thermoplasmonic effect is triggered by the plasmon excitation of the metal nanoparticles that provokes first the generation of hot carriers in the metal nanostructure at a very short time scale (1-100 fs). Then, thermalization of the NP occurs by electron-electron scattering and electron-phonon scattering and the produced heat can then dissipate to the surrounding medium by heat diffusion. Detailed description of this phenomenon can be found in **[39]**. However, when changing the substrate from glass to resin, we need to reduce the laser intensity or irradiation time to avoid burning the substrate. The well-dispersed Au NPs were not successfully formed.

In this study, we successfully overcame the previous problem to propose a visible light PD on the 3D-printed resin. The integration with a biochemical reactor to

detect urea concentration was also demonstrated. The key to realize the NIR laser-annealed Au NPs/IZO PD on the 3D-printed substrate was the critical match of the Au film thickness and the laser power intensity. With the limited thermal endurance of the resin substrate, the initial Au thin film has to be thick enough to absorb NIR laser for forming the Au NPs by melting the Au film. At the same time, the heating has to be suppressed to avoid damaging the substrate. In this work, the Au film thickness is well adjusted as the first step. The thermal imager was also found to be an effective tool to reflect the real-time temperature profile during the NIR laser irradiation and hence to define the suitable laser irradiation conditions. With well-formed Au NPs to serve as the aforementioned nanoheaters, the following IZO layer can then be formed to exhibit good enough conductivity with only 3 min NIR laser annealing (16.4 $W \cdot cm^{-2}$). Finally, the optimized Au NPs/IZO PD was successfully integrated with a 3D-printed sensing chamber as a miniaturized biosensor with a total thickness less than 5 mm for demonstrating colorimetric urea sensing. Salivary urea has been indicated as one of the non-invasive biomarkers for chronic kidney disease (CKD) screening (normal group: 2~6 mM, CKD group: >10 mM) **[40-42]**, our proposed biosensor was able to offer suitable sensitivity with equivalent urea concentration varied from 1, 5, 10, 25, and 50 mM.

2. Experimental Section:

2.1 Resin substrates preparation:

In this work, there are 3 kinds of resin substrates in total (**Fig. 1(a)**), including one molded (named as Substrate-I) and two 3D-printed substrates (named as Substrate-II, Substrate-III) prepared from a UV curable (385 nm or 405 nm) methacrylate-based

resin (Ackuretta Curo Splint). Using the photopolymer bisphenol A-ethoxylate dimethacrylate (Bis-EMA) **[43]**, substrates with relatively high glass transition temperature (Tg) and good transparency for reducing substrate damage during NIR laser annealing processes were expected. Besides, all the substrates were prepared with a thickness as 1 mm.

Substrate-I was prepared by a molded process as shown in Flow-I in Fig. 1(a). After filling the resin in a glass-made mold with a cover glass, the mold was then put into a UV light box (designed from ORIENT SERVICE CORP.) with 10 min curing. Finally, molded resin substrates with smooth surfaces were obtained after demolding.

To fabricate Substrate-II and Substrate-III, we used the printed-model from the 3D stereolithography printer (Sonic mini 4K (Phrozen TECH CO, LTD)). After the substrate was printed, Substrate-II was rinsed by ethanol before post-curing in a UV lamp chamber (Phrozen Cure (Phrozen TECH CO, LTD)) for 5 min as shown in Flow-II. Obvious wrinkles were observed on the surface, which aligned with the printing direction. In Flow-III, to planarize the surface, before entering the UV post curing box, the printed substrates were coated with Bis-EMA resin and were pressed by 2 glass sheets from the two sides. A smooth 3D-printed substrate was obtained, named as "Substrate-III".

.

2.2 Materials for preparing sol-gel IZO precursor solution:

Indium nitrate (indium(III) nitrate hydrate, 99.9%, Sigma-Aldrich), zinc nitrate (zinc nitrate hexahydrate, ≥99.0%, Sigma-Aldrich) were mixed with molar ratio as 5:4. Then, the mixture was dissolved in 2-methoxyethanol (2-MOE, ≥99.9%, Sigma-Aldrich) with total concentration as 0.25 M. After 24 h stirring at room temperature, the solution was further used for synthesizing the photoactive Au NPs/IZO thin film

based on sol-gel method.

2.3 The fabrication of full NIR laser-annealed Au NPs/IZO PD on resin substrates

The Au NPs/IZO PDs were fabricated by a NIR continuous wave laser (808 nm, beam size: 5 mm × 5 mm, DS3-11312-xxx-LD No, BWT 135 Beijing) with 2 main NIR laser annealing stages (**Fig. 1(b)**). Noted that such 2 stage NIR laser annealing was also applied on our previous published PD on glass substrate. Here we need to adjust the condition to realize PD on resin substrates. Firstly, in Stage A, after a layer of Au thin film was deposited by thermal evaporation, the 1st NIR laser annealing process was adopted by locally melting Au thin film for forming Au NPs. Then, in Stage B, Au NPs were covered by sol-gel IZO precursor solution by spin-coating with a following low temperature heating process at 60 ^{o}C for 10 min. The 2nd NIR laser annealing process was applied on samples for sol-gel IZO thin film curing. Finally, Au electrodes (size: 1.2 mm × 1.2 mm, interval: 200 μm, and thickness: 20 nm) were deposited through a shadow mask by thermal evaporation to finish the PD.

During measurement, 4 LEDs (410 nm (26 mW·cm^{-2}), 465 nm (521 mW·cm^{-2}), 515 nm (226 mW·cm^{-2}) and 630 nm (226 mW·cm^{-2})) were adopted for evaluating the UV-vis photoresponsivities of all Au NPs/IZO PDs in this work.

2.4 The 3D-printed sensing chamber for colorimetric sensing

In order to develop a miniaturized biosensor composed by integrating the NIR laser-annealed Au NPs/IZO PD fabricated on 3D-printed resin substrate for demonstrating colorimetric sensing, a compact 3D-printed sensing chamber (diameter: 3.5 cm, thickness: 4 mm) with comparable size as a coin was then designed. From **Fig. 1(c)**, the sensing chamber was printed with 4 solution tanks

(diameter: 5 mm, depth: 3 mm for each), and a photo-detecting cover could be prepared by fabricating the PD on the printed Substrate-III with the area as 2.2 cm × 2.2 cm.

To demonstrate colorimetric urea detection, the colorimetric urea solution samples were prepared by mixing 3 kinds of solutions, including urea solution, urease (enzyme) solution, and phenol red (pH indicator) solution. The preparation of the three solutions were as follows. The urea solution was prepared by dissolving urea pellets (J.T.Baker) in deionized (DI) water. To reflect the dilution step in many real tests, the urea solution is 100 times diluted from the targeted sensing concentrations as 0, 1, 5, 10, 25 and 50 mM, named as the equivalent concentration. The urease solution was prepared by dissolving urease (Type IX, powder, 50,000-100,000 units/g solid, Sigma-Aldrich) in DI water with concentration as 2.1×10^{-4} wt%. The phenol red solution was prepared by mixing 0.1 g phenol red (Alfa Aesar) and 5.7 ml sodium hydroxide (NaOH) solution (0.05 M) with DI water filled till 250 ml in total.

After mixing all the 3 solutions with a fixed ratio (3 ml urea solution, 0.1 ml urease solution, and 0.2 ml phenol red solution), the saturated colorimetric samples could then be prepared by following the chemical reaction as **(1) [44]** due to the change in pH value.

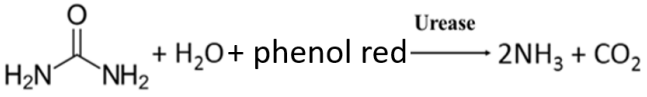

(1)

The measurement was conducted by integrating the optimized NIR laser-annealed Au NPs/IZO PD, an LED, and the 3D-printed sensing chamber filled with colorimetric urea samples as **Fig.1 (d)**, the results will be discussed in section 3.4.

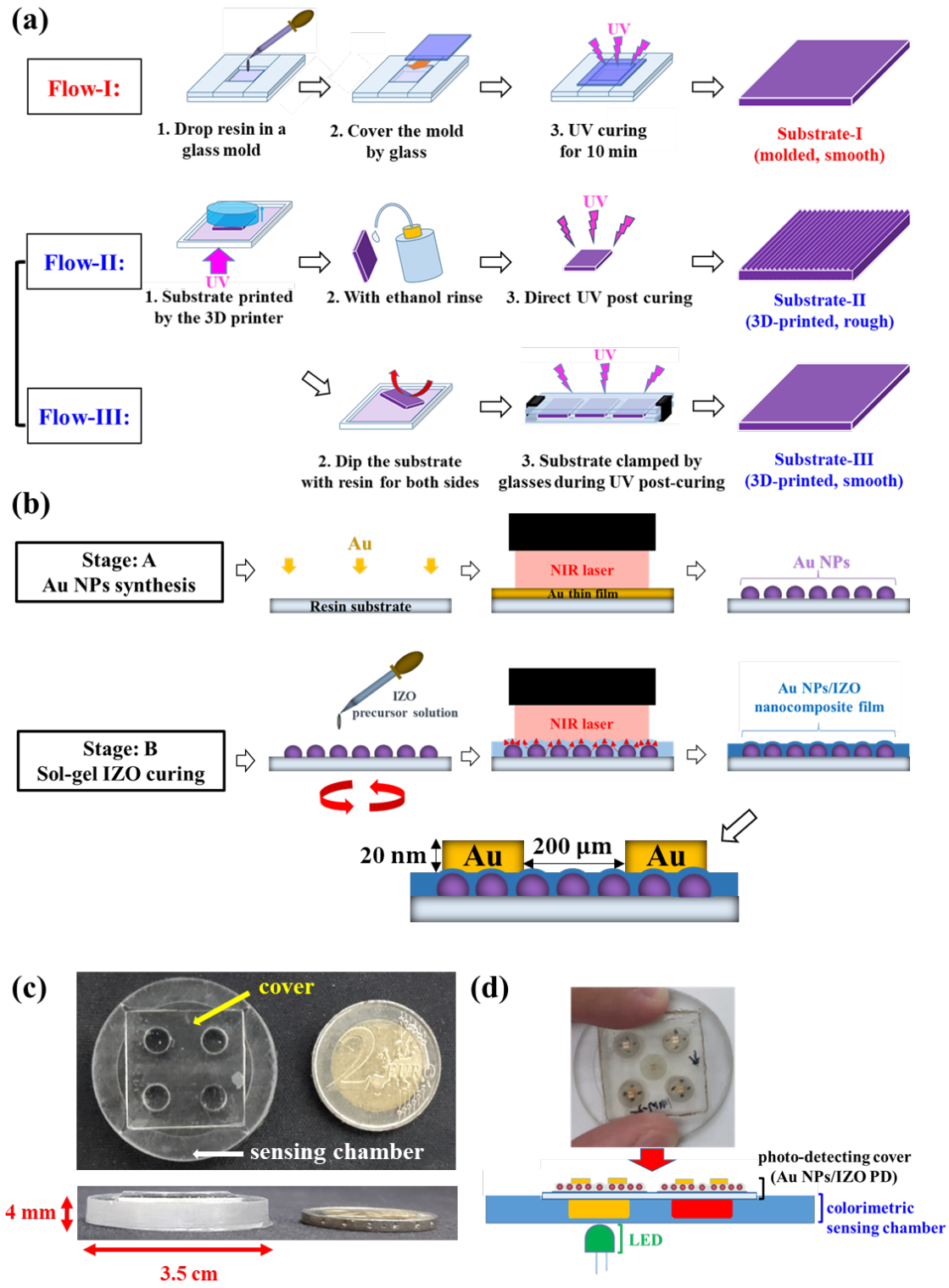

Fig. 1: The preparation methods of (a) 3 kinds of resin substrates; (b) the 2 main Stages of NIR laser annealing for forming Au NPs/IZO PD; (c) the 3D-printed biosensor composed by a cover and a sensing chamber; (d) the schematic image of vertically-integrated biosensor for colorimetric sensing

3. Results and discussion:

3.1 NIR laser-annealed Au NPs/IZO PD on Substrate-I (molded)

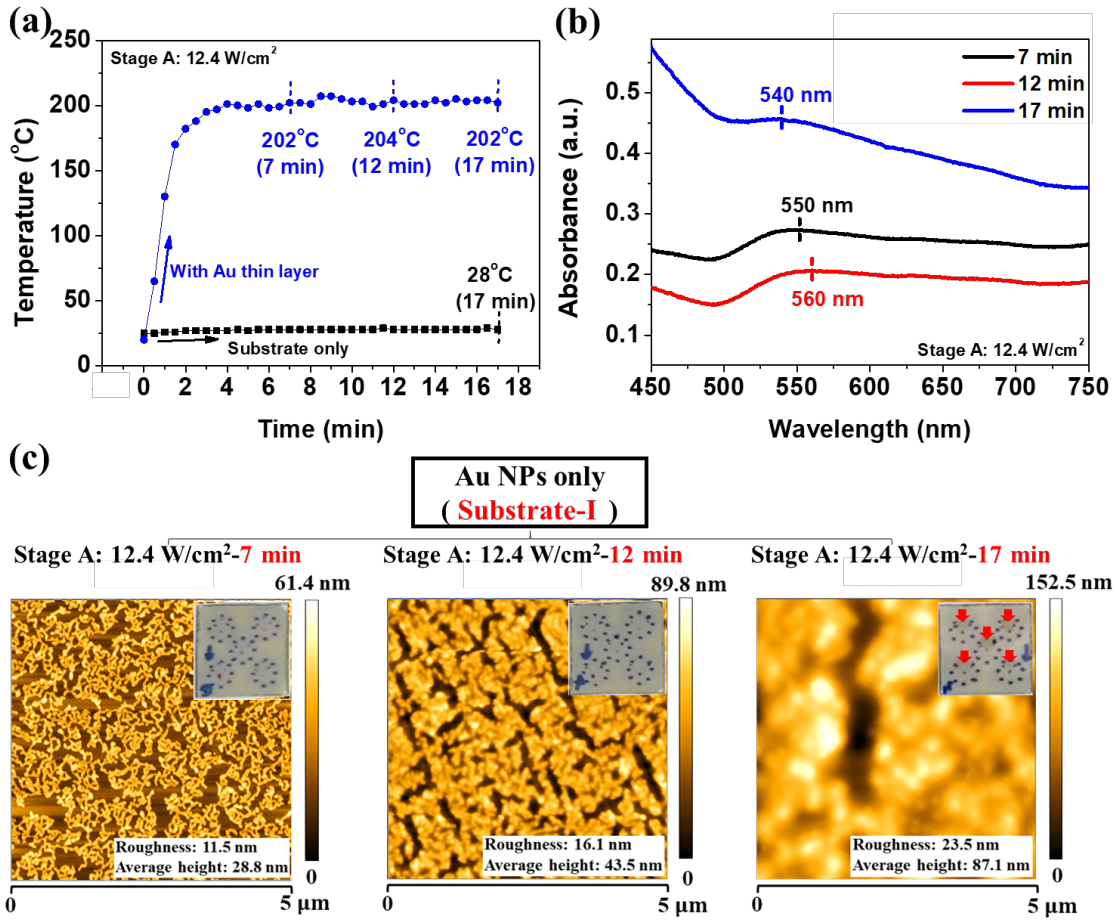

Fig. 2: (a) The temperature profile (b) the corresponding absorption spectra of Au NPs with substrates (c) the surface morphology of Au NPs formed by Stage A: 12.4 W·cm^{-2} with process time from 7 min to 17 min on Substrate-I (with treated parts marked)

In our previous work **[38]**, the main problem to realize the visible light PD on the 3D-printed resin substrates was due to the substrate burning when forming the Au NPs. Here we modulate the initial thickness of Au thin layer since it dominates the

NIR laser absorption for producing heat to melt the Au film for forming Au NPs. The absorption spectra corresponding to various Au film thickness (6 nm to 16 nm) are shown in **Fig. S1**. With an overview of each spectrum, the absorbance in NIR wavelength range gradually enhances when the wavelength increases. To properly control the heating effect of NIR laser annealing, the 808 nm laser was thus applied to conduct the Au NPs preparation. Indeed, after testing other wavelengths in the visible (532 and 633 nm) and infrared (1300 and 1550 nm) range, it appears that 808 nm is a good compromise to obtain sufficient power densities for an efficient curing during Stage A and B, but without generating damage to the polymer substrate. For the 6-nm-thick Au film, the absorbance at the 808 nm (NIR laser wavelength) is much lower than the absorbance in other thicker samples. We hence introduce 6-nm-thick Au film in the following tests to check if the well dispersed Au NPs with the LSPR effect can still be obtained on the resin substrate. In this section, the molded **Substrate-I** was chosen to do the preliminary test. On such substrates, the feasibility on resin material can be demonstrated without considering the printing-induced texture effect. The molded Substrate I exhibits a smooth surface (Roughness < 1 nm) as shown in the AFM image (Genie AFM, Force) in **Fig. S2(a)**.

First, appropriate NIR laser treatment conditions to form suitable Au NPs were defined. The well dispersed Au NPs need to be formed. Also, the substrate temperature cannot be too high to burn the substrate. After depositing Au thin layer on Substrate-I, Stage A with fixed power intensity as 12.4 $W \cdot cm^{-2}$ was adopted. Besides, a thermal imager (Testo 875i - versatile) was used for investigating the thermal effect induced during NIR laser treatments. By focusing on the substrate, the real-time analysis of highest surface temperature variation could then be recorded by the thermal imager. Also, to obtain adequate time for image saving, a time period was

kept as 30 sec in between of each image capture. In **Fig. 2(a)**, the substrates with or without Au thin layer are compared. The surface temperature on blank substrate has almost no change during 17 min laser irradiation (black curve). The one with Au increases rapidly from room temperature to 200 ^{o}C in around 4 min, and it then keeps staying at the same temperature until 17 min (blue curve). The local heating phenomenon could also be found on the sample with the area as 5 mm × 5 mm corresponding to the size of laser beam, as shown in **Fig. S2(b)**. With heat generated from NIR laser irradiation, Au NPs are formed from Au film based on the phenomenon of Rayleigh instability **[45,46]**. Thus, the analysis for investigating the formation of NIR laser annealed-Au NPs with processing time of 7 min, 12 min and 17 min are then offered in **Fig. 2(b)** and **Fig. 2(c)** by separately using the UV-vis spectrometer (AvaSpec-ULS2048CL-EVO) and atomic force microscopy (AFM, Molecular Imaging PicoPlus (resonant mode)).

In **Fig. 2(b)**, the absorption spectra of NIR laser annealed-Au NPs on molded resin substrates with laser annealing time as 7 min, 12 min, and 17 min are shown. The three samples (7 min, 12 min, and 17 min laser treat) all exhibit LSPR absorption phenomenon and the corresponding absorption peaks at 550 nm (7 min), 560 nm (12 min), and 540 nm (17 nm), respectively. The surface morphology for NIR laser annealed-Au NPs (AFM images) is shown in **Fig. 2(c)**. With 7-min laser annealing (the left image in **Fig. 2(c)**), the sample color changes from olive to purple and nano-islands with Au NPs are gradually generated by melting Au film. The resulting surface roughness is 11.5 nm and the average height is as high as 28.8 nm due to the capillary instability. As the laser processing time extends to 12 min (the center image in **Fig. 2(c)**), the higher density of Au NPs then contributes to the slightly increased surface roughness of 16.1 nm with an average height of 43.5 nm. A redshift of LSPR

absorption peak is also obtained in **Fig. 2(b)**. However, as the laser processing time extends to 17 min, the burnt parts with brown color on the substrate (marked by red arrows) start to be generated. Even though the formation of Au NPs can still be speculated by showing the LSPR absorption peak in **Fig. 2(b)**, the burnt parts with melted and cracked surfaces finally lead to greatly increased surface roughness of 23.5 nm with an average height of 87.1 nm. To further assist the morphological analysis of Au NPs, a scanning electron microscope (SEM) system of JSM-7900F from JEOL was applied. The SEM images corresponding to the three Stage A annealing conditions of **Fig. 2(c)** are respectively shown in **Fig. S3(a)** to **Fig. S3(c)** (×10000 magnification). Also, the images with higher magnification (×50000) of **Fig. S3(a)** and **S3(b)** are respectively shown in **Fig. S3(d)** and **Fig. S3(e)**. The morphological analysis in SEM images agrees with the analysis results from the AFM images. Therefore, in order to reach a better surface condition for sol-gel IZO film coating, the NIR laser-annealed Au NPs with processing time of 7 min and 12 min were chosen for the following PD fabrication.

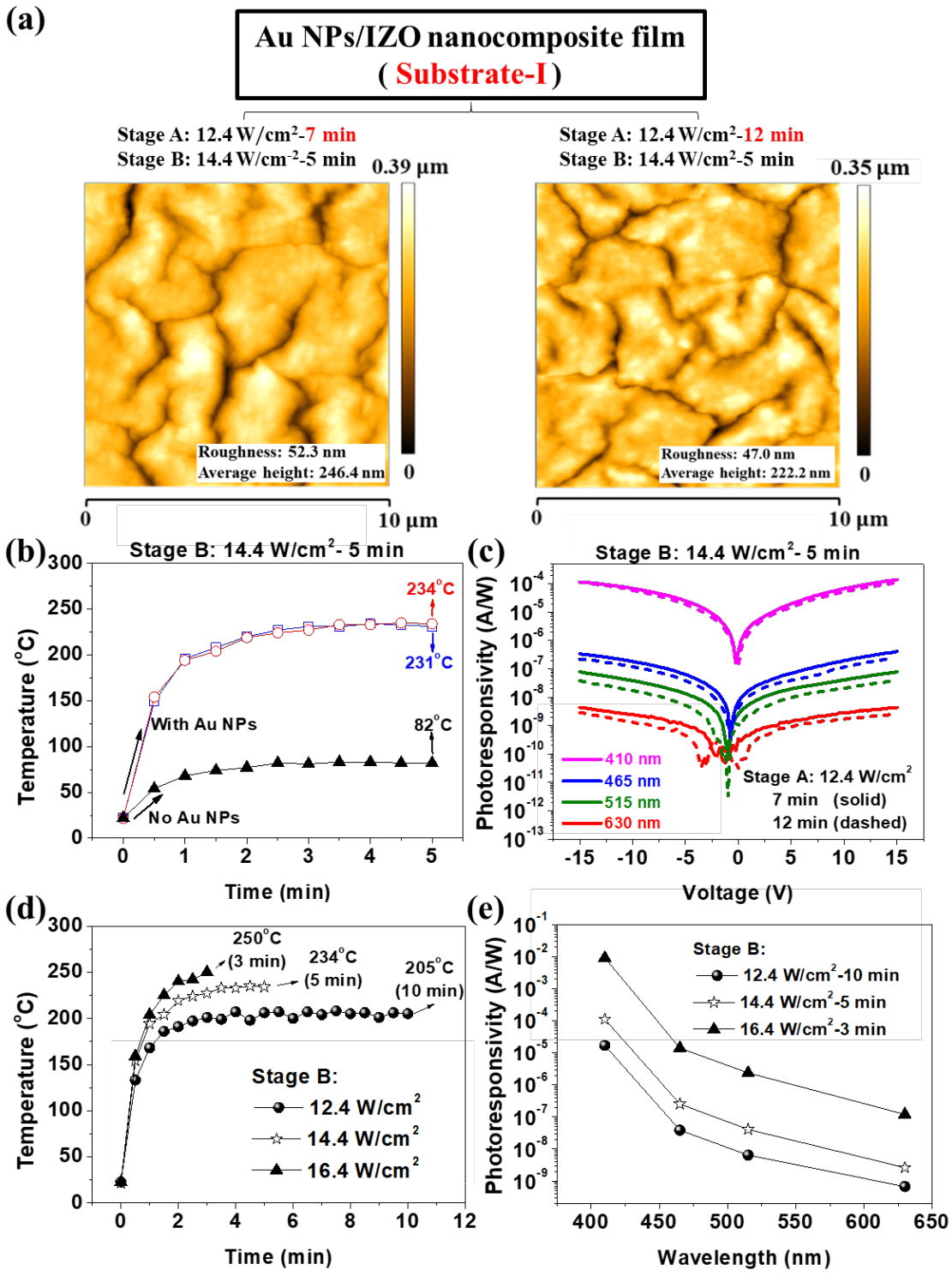

Fig. 3: The comparison of NIR laser-annealed Au NPs/IZO nanocomposite film ((Stage A: 12.4 W·cm^{-2}-7 or 12 min), (Stage B: 14.4 W·cm^{-2}-5 min)) on Substrate-I, including (a) surface morphology (b) temperature profile of Stage B with/without Au NPs (no Au NPs (black), Stage A: 12.4 W·cm^{-2}-7 min (blue), 12 min (red)) (c) UV-vis photoresponse of PD; The comparison of NIR laser-

annealed Au NPs/IZO nanocomposite film ((Stage A: 12.4 W·cm^{-2}-12 min), (Stage B: 12.4 W·cm^{-2}-10 min, 14.4 W·cm^{-2}-5 min, or 16.4 W·cm^{-2}-3 min)), including (d) temperature profile for Stage B (e) UV-vis photoresponse of PD (bias voltage: 15 V), all with IZO coating: 2000 rpm-50 sec

In order to further synthesize the visible photoactive Au NPs/IZO nanocomposite thin film based on sol-gel process, it's been indicated that appropriate thermal energy is required for leading the hydrolysis and condensation reaction based on thermogravimetric analysis (TGA) **[47]**. Then, M-O network can be transformed from metal alkoxides by removing those decomposed volatile residues, including water molecules and organic groups. In our work, when NIR laser annealed-Au NPs were formed on molded resin substrates by Stage A, Stage B was then adopted after coating sol-gel IZO precursor solution for forming the Au NPs/IZO nanocomposite thin film. Based on thermoplasmonic effect, heat is able to be induced by LSPR absorption on Au NPs, and the level tuned by laser irradiation conditions of Stage B was found to efficiently improve the photoresponsivities of Au NPs/IZO PD displayed in **Fig.3**.

In **Fig. 3(a)**, the AFM images of the IZO films on 2 molded resin substrates with different Au NP conditions (the 7 min and the 12 min treated Au NPs in Stage A) were firstly compared. The IZO film was formed by spin-coating sol-gel precursor solution with the following NIR laser annealing (Stage B, 14.4 W·cm^{-2}-5 min). We noticed that no obvious morphology difference can be found even when the underlying Au NPs exhibit different morphology as in **Fig. 2(c)** (left and center images). During the 5-min Stage B laser annealing, the surface temperature profile was traced as shown in **Fig. 3(b)**. A control sample with IZO film but without the Au NPs layer was also fabricated and traced. Obviously, in the control sample (black

color data), without the heat generated by thermoplasmonic effect from Au NPs for sol-gel IZO curing, the surface temperature can only reach a terminal temperature of 82 ^{o}C which is much lower than the temperature needed to form the M-O network. As a result, almost no photoresponse could be found in the control sample (**Fig. S4(a))**. On the contrary, for the other 2 samples with Au NPs for sol-gel IZO curing, since the LSPR characteristics of Au NPs are similar, their surface temperatures increase much faster, and then achieve at around 230 ^{o}C. The UV-vis photoresponsivity values for these two PDs are also shown in **Fig. 3(c)**. The photoresponsivity was calculated according to equation **(2) [48]** from the original current-voltage characteristics in dark and under light irradiation (in **Fig. S4(b)** and **Fig. S4(c)**). The Au NPs/IZO PD with 7-min-treated Au NPs show a bit higher photoresponsivity than the Au NPs/IZO PD with 12-min-treated Au NPs. This agrees with the absorption spectrum shown in **Fig. 2(b)** that the 7-min-treated Au NPs exhibit a higher absorption then the 12-min-treated Au NPs.

$$\text{Photoresponsivity} = \frac{{I_{light} - I_{dark}}/{Area\ of\ PD}}{{Power\ of\ light\ source}/{Area\ of\ light\ source}} \quad (2)$$

Additionally, we'd like to discuss the influence of tuning sol-gel IZO curing conditions on the corresponding photoresponsivities. The samples have the same Stage A condition (12.4 W·cm^{-2}-12 min laser annealing), and 3 different Stage B conditions (12.4 W·cm^{-2}-10 min, 14.4 W·cm^{-2}-5 min, or 16.4 W·cm^{-2}-3 min). The surface temperature profile and the photoresponsivity of the 3 samples are shown in **Fig. 3(d)** and **Fig. 3(e)**, respectively. The corresponding I-V curves are given in **Fig. S4(c) to Fig. S4(e)**. As shown in **Fig. 3(d)**, increasing laser intensity leads to a faster temperature rise and hence a shorter irradiation time without burning the resin substrate. Even with the reduced laser irradiation time, in the UV-vis photoresponsivity (**Fig. 3(e))** of NIR laser-annealed Au NPs/IZO PD can still be

improved by increasing the NIR laser annealing power intensity for leading higher surface temperature (**Fig. 3(d)**). Finally, the improved UV-vis photoresponsivity (410 nm: 9.2×10^{-3} A/W, 465 nm: 1.4×10^{-5} A/W, 515 nm: 2.4×10^{-6} A/W and 630 nm: 1.2×10^{-7} A/W) can be performed by adopting 16.4 W·cm^{-2}-3 min for Stage B with the maximum surface temperature as 250 °C.

3.2 The comparison of NIR laser-annealed Au NPs/IZO PDs on Substrates-I, II and III

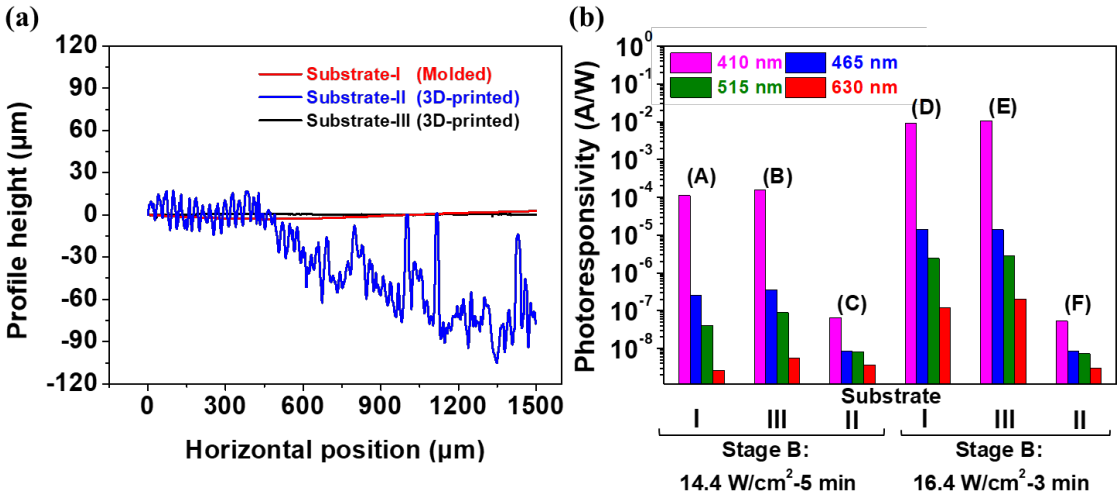

Fig. 4: The comparison of (a) profile height variation and (b) UV-vis photoresponsivities (bias voltage: 15 V) of NIR laser annealed-Au NPs/IZO PDs ((Stage A: 12.4 W·cm^{-2}-12 min), (Stage B: 14.4 W·cm^{-2}-5 min, or 16.4 W·cm^{-2}-3 min)) fabricated on Substrate-I, II and III, all with IZO coating: 2000 rpm-50 sec

After investigating the feasible conditions of fabricating NIR laser annealed-Au NPs/IZO PD on Substrate-I, in this section, the PD fabrication was then directly tested on 3D-printed substrates. Also, the impact of substrate morphology for PD performance will be discussed. From the different preparation flows in section 2.1, there are 2 kinds of 3D-printed substrates prepared in this work, one is the pristine

printed substrate (Substrate-II) and the other has an additional planarization step (Substrate-III). The large-scale (1500-μm) surface profiles (profilometer: DektakXT, Bruker) for the two substrates were compared in **Fig. 4(a)**. The rough surface with wrinkles can lead to height variation with tens of micrometers (Maximum: 89.18 μm) on the pristine printed Substrate-II. For Substrate-III, the surface roughness can successfully be reduced to the comparable level as Substrate-I. Apparently, the planarization process works effectively for obtaining a smooth surface.

Then, the influence of substrate roughness on the performance of Au NPs/IZO PD was investigated. We fabricated PDs with Stage B laser treatment conditions as 14.4 W·cm^{-2}-5 min on Substrate-I, III and II, named as samples (A), (B), and (C), respectively. Also, PDs with the other Stage B laser treatment condition (16.4 W·cm^{-2}-3 min) on Substrate-I, III and II were fabricated and named as samples (D), (E), and (F), respectively. The corresponding photoresponsivities of the 6 PDs are compared in **Fig. 4(b)**. On the rough Substrate II, samples (C) and (F) have much lower photoresponsivities. Improved photoresponsivities with almost the same values were found in samples (A) and (B), also in samples (D) and (E). This indicates that when the PDs fabricated on smoothened substrates with similar surface roughness (Maximum height difference in 1500-μm horizontal scanning: 5.63 μm in Substrate-I and 2.84 μm in Substrate-III), almost identical UV-vis photoresponsivity are obtained. This also verifies that the planarization process is critical when fabricating PDs on the printed substrates. Besides, the photoresponsivities in samples (D)(E) are higher than in samples (A)(B). This tells that increasing the Stage B NIR laser power density for sol-gel IZO curing, the UV-vis photoresponsivity can be further improved.

For the PDs on the rough Substrate-II, it's obvious to find the strong decrease of UV-vis photoresponsivity. Even increasing Stage B laser power density in sample (F)

does not improve the photoresponsivity as compared with sample (C). Since the IZO film thickness analyzed by the ellipsometer (HORIBA UVISEL) is only 25 nm by adopting the same spin-coating condition as 2000 rpm-50 sec on glass, such thin film was not able to cover well on the rough Substrate-II surface, leading to the poor PD performance. Noted that when increasing the IZO film thickness to be 45 nm, the conduction current level on Substrate II remains low while that on Substrate III obviously increases. The thick Au NPs/IZO PDs will be discussed in the following section.

3.3 The optimization of NIR laser-annealed Au NPs/IZO PDs on Substrate-III by tuning IZO film thickness

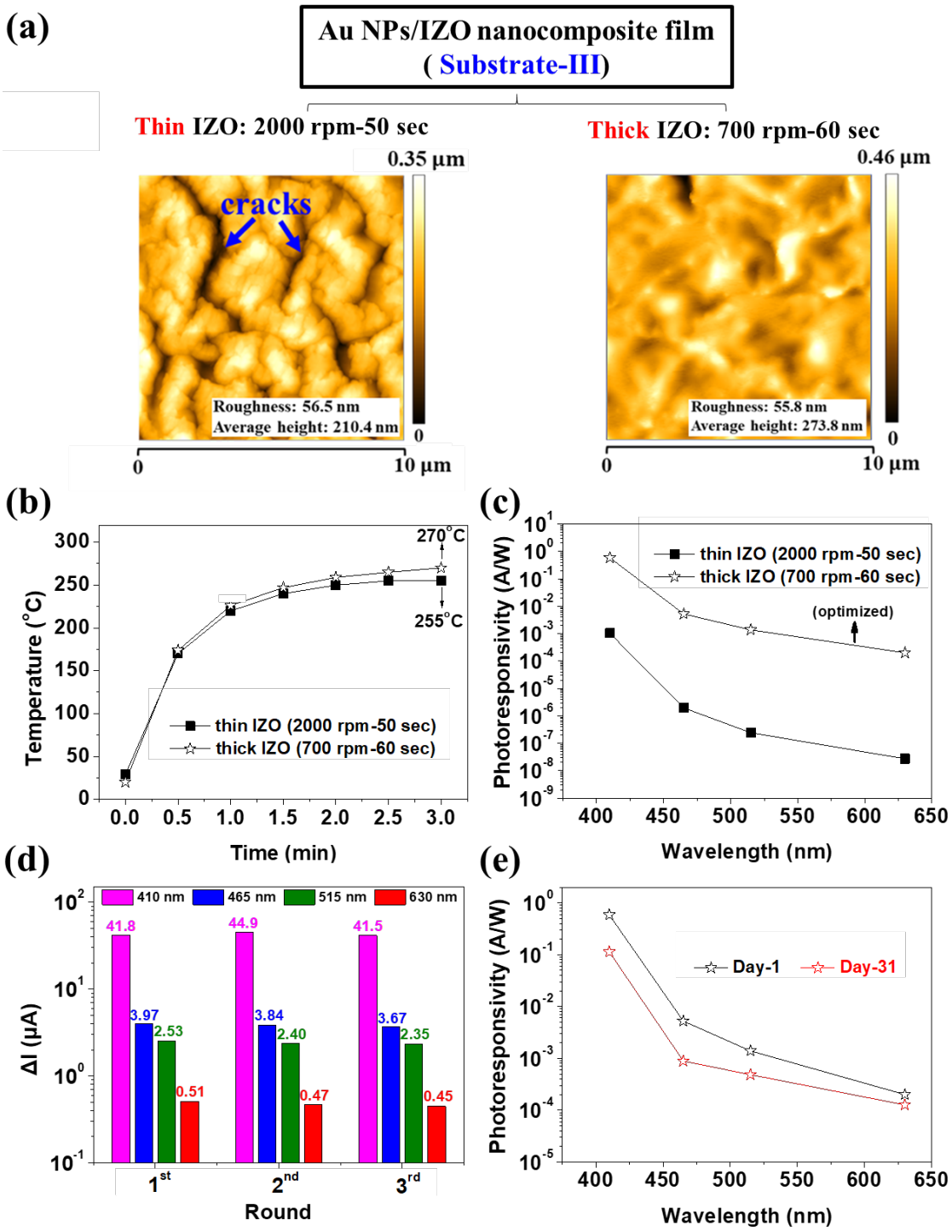

Fig. 5: NIR laser-annealed Au NPs/IZO PDs ((Stage A: 12.4 W·cm^{-2}-7 min), (Stage B: 16.4 W·cm^{-2}-3 min)) fabricated on Substrate-III with thin (2000 rpm-50 sec) or thick (700 rpm-60 sec) IZO coating, (a) the surface morphology of Au NPs/IZO nanocomposite film (b) the temperature profile for Stage B (c) the corresponding UV-vis photoreponse (bias voltage: 15 V); (d) the dynamic UV-vis

photoresponse (1 cycle: 1 min light irradiation + 6 min light off) and (e) the lifetime performance (bias voltage: 15 V) of thick IZO PD

From previous section, it's noticed that IZO film quality may be an important factor relating to the photoresponsivity of NIR laser-annealed Au NPs/IZO PD. We here like to discuss the feasibility of further improving the PD performance by tuning IZO film thickness. In this section, Substrate-III is used based on its smooth surface with reduced printing-induced texture.

To prepare the Au NPs/IZO PDs, two samples were fabricated by identical NIR laser annealing conditions (Stage A as 12.4 $W \cdot cm^{-2}$-7 min, Stage B as 16.4 $W \cdot cm^{-2}$-3 min), but the spin-coating speed of IZO film was adjusted from 2000 rpm-50 sec (thin) to 700 rpm-60 sec (thick) for obtaining different IZO film thickness. As a reference, on glass substrate, the two spin-coated IZO films with 2000 rpm-50 sec and 700 rpm-60 sec conditions exhibit the thickness as 25 nm and 45 nm, respectively. First, the AFM images of the two Au NPs/IZO nanocomposite films displayed in **Fig. 5(a)** were checked. Although the surface roughness values are similar, the film continuity is obviously improved by increasing IZO film thickness with reduced cracks (the right image). The temperature profiles during Stage B laser treatment are shown in **Fig. 5(b).** With thick IZO film coating, temperature also increases faster, and the maximum reaches a higher temperature at 270 ^{o}C after 3-min laser irradiation. This suggests a stronger thermoplasmonic effect induced by higher light absorption from thicker Au NPs/IZO nanocomposite film. As a result, for the thick-film PDs, an improved IZO film quality **[49]** was obtained due to the increased thermal energy for sol-gel IZO curing. The comparison of the photoresponsivity of the thin and thick Au NPs/IZO PDs were shown in Fig. 5(c) and the I-V curves were provided in **Fig. S5(a)**

and **Fig. S5(b)**. The increase of IZO thickness may also improve the light absorption and reduce channel resistance. However, as shown in **Fig. 5(c)**, the photoresponsivity in the thick IZO device was enlarged throughout the wavelength from 410 nm to 630 nm. We know that IZO film mostly absorbs UV or blue light and does not absorb red light. Hence, we can rule out the effect of increased light absorption in thick IZO film. The thick film may also reduce the channel resistance and contribute to the current increase. However, in **Fig. S5(b)**, the dark current in thick (45 nm) IZO device is about 4 orders larger than that in thin (25 nm) IZO device. Hence, we propose that the film quality improvement dominates the greatly enlarged conductivity and hence the increased photoresponsivity. Specifically speaking, the optimized UV-vis photoresponsivities are 5.9×10^{-1} A/W for 410 nm, 5.2×10^{-3} A/W for 465 nm, 1.4×10^{-3} A/W for 515 nm, and 2.0×10^{-4} A/W for 630 nm.

After characterizing the optimized Au NPs/IZO PD, we further investigated other important properties such as the dynamic light detection and the operation lifetime. In **Fig. 5(d)**, we used 4 different LEDs (illumination peak wavelength: 410 nm, 465 nm, 515 nm and 630 nm) with 3 repeating irradiation cycles (1 min irradiation and 6 min light off for each) for examining dynamic light detection properties. Apparently, almost consistent results can be respectively collected from the current variation (ΔI) values presented for each LED. Subsequently, for evaluating the operation lifetime, the PD can even be stably operated for more than 1 month from the performance shown in **Fig. 5(e)**. Based on the detailed investigation with good photo detecting properties, we confirm the suitability of integrating the PD for demonstrating colorimetric sensing.

Moreover, the optimized photodetection properties of NIR laser-annealed Au NPs/IZO PD is compared with recent works of PDs fabricated on flexible or 3D-

printed substrates in Table 1. Obviously, by photo-induced thermoplasmonic effects, the NIR laser treatments can efficiently complete photoactive layer curing at low surface temperature in a much shorter treatment time. Especially, the Au NPs/IZO nanocomposite photoactive layer also benefits the wide UV-vis light detection range, good photoresponsivities, and long operation lifetime. Based on these excellent characteristics, except for spin coating, if the printing coating technics (e.g. ink-jet printing **[50-54]**, extrusion-based printing **[55]**, syringe printing **[56,57]** or solution dripping **[58]**) proposed from other works in Table 1 for depositing photoactive layer are assisted, our NIR laser-annealed Au NPs/IZO PD fabrication is also potential to be extended on various 3D printed designs with functional applications.

	Active layer coating	**Photoactive material**	**Annealing temperature/time**	**Substrate**	**Photoresponsivity (A/W)**	**Lifetime (Day)**
Our work	**Spin coating**	**Au NPs/ IZO (sol-gel)**	**270 °C (terminal)/3 min (NIR laser annealing)**	**3D printed resin (Bis-EMA based)**	**5.9×10^{-1} (410 nm) 5.2×10^{-3} (465 nm) 1.4×10^{-3} (515 nm) 2.0×10^{-4} (630 nm)**	**≥30**
[50]	Ink-jet printing	WS_2	80 °C (vacuum)/--	PEL P60 paper	6.1×10^{-4} (532 nm)	--
[51]		ZnO (sol-gel)	239 °C/5 min (DC micro-heater)	Si/SiO_2 substrate	2.9×10^{-2} (365 nm)	--
[52]		ZnO (sol-gel)	200 °C/10 min and 400 °C/60 min (post heat)	polyimide	$\sim1.7\times10^{-3}$ (370 nm)	--
[53]		MoS_2	330°C/3 h		$\sim3\times10^{-1}$ (Broadband light)	--
[54]		Organohalide perovskite	100 °C/30 min		$\sim1.7\times10^{-1}$ (750 nm)	13 (glove box)
[55]	3D-printing (extrusion-based)	P3HT:PCBM	--/--	PET or hemispherical glass dome	$\sim8\times10^{-2}$ (510 nm)	--
[56]	3D printing (syringe)	P3HT (NWs) with epoxy	Room temperature (vacuum)/--	ITO glass or wood, cardboard, glass fiber cloth	$\sim2\times10^{-2}$ (Broadband light)	--
[57]		ZnO (NPs)	Room temperature/24 h	3D-printed polyurethane (TPU)	$\sim1.5\times10^{-3}$ (365 nm)	--
[58]	Solution dripping (PDMS mask)	SnO_2-CdS (NWs)	60 °C/4 h	PDMS	$\sim1.5\times10^{-7}$ (370 nm)	--
		ZnO-CdS (NWs)			$\sim5\times10^{-4}$ (370 nm)	

Table. 1: The compilation of PDs fabricated on flexible or 3D-printed substrates by printing technics for photoactive layer coating

3.4 The integrated 3D-printed sensing chamber for colorimetric urea detection

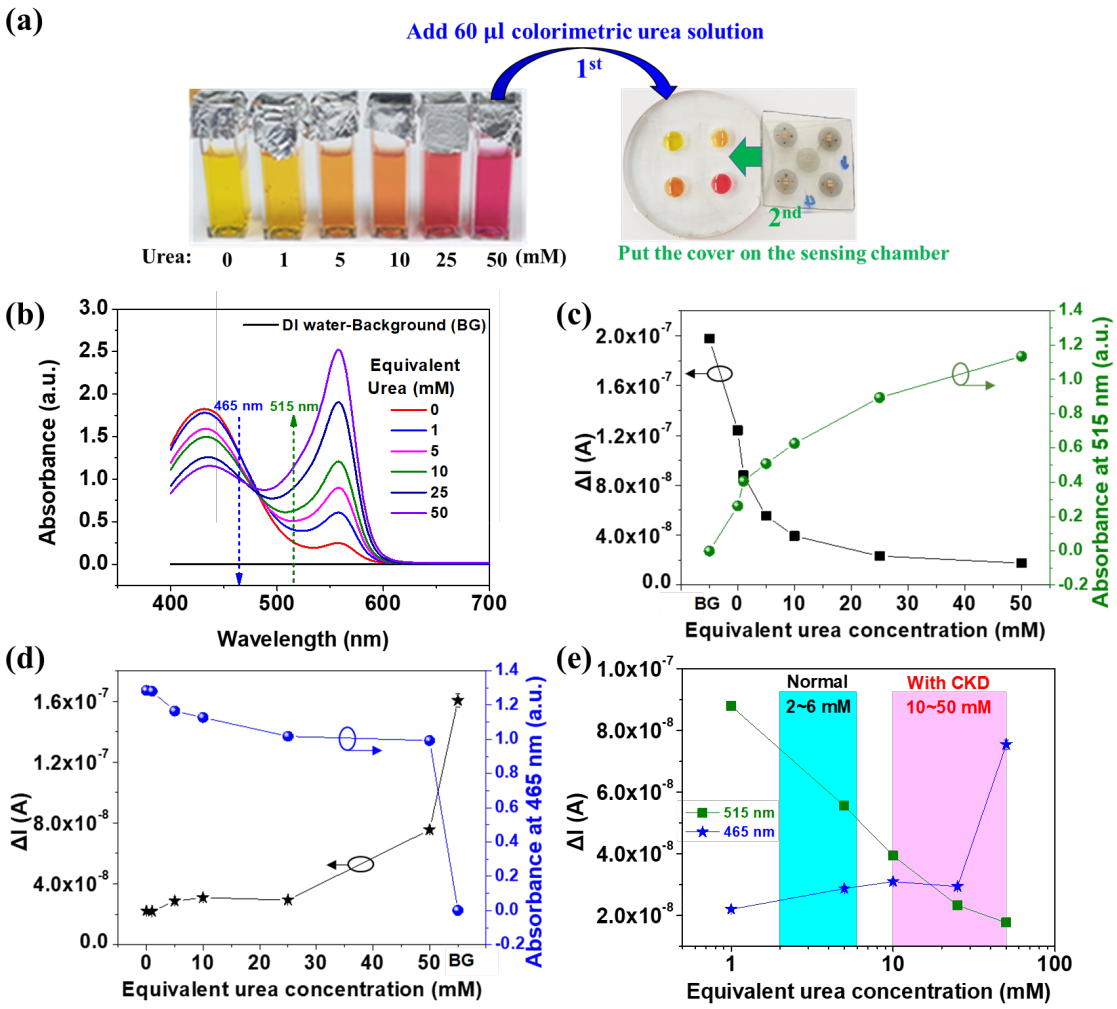

Fig. 6: (a) Photographs of the urea solutions and 3D printed chamber with PD cover (b) the absorption spectra of colorimetric samples with equivalent urea concentration varied from 0, 1, 5, 10, 25, 50 mM; the calibration curves of the vertically-integrated biosensor demonstrated for colorimetric urea detection with corresponding wavelength at (c) 515 nm (d) 465 nm and (e) the evaluation for CKD of human beings

In the last section, the optimized NIR laser-annealed Au NPs/IZO PD fabricated on Substrate-III as the photo-detecting cover was finally integrated with the

3D-printed sensing chamber (**Fig. 6(a))**. First, the colorimetric urea solution samples were prepared by following the ways introduced in section 2.4 with equivalent concentration varied from 0, 1, 5, 10, 25, 50 mM. Obviously, the color can be tuned from yellow to pink by increasing the urea concentration. To basically quantify these colorimetric samples, here the UV-vis spectrometer (VARIAN Cary 50 Scan UV/Vis Spectrophotometer) was also used to assist the analysis, and the corresponding UV-vis spectra are displayed in **Fig. 6(b)**. In the wavelength range of 480-620 nm, an absorbance peak is observed at 558 nm. The absorbance of this peak increases when increasing urea concentration. In the range of 400-480 nm, a peak at 430 nm is observed, with an absorbance decreasing with urea concentration. An isosbestic point is observed at 480 nm in agreement with the reaction between these two species. The urea concentration measurements can thus be carried out by following this two peaks, using different light sources. Therefore, to evaluate the sensitivity of our vertically-integrated biosensor, 2 commercial LEDs that we previously used for evaluating the photoresponsivity of Au NPs/IZO PD were considered, one with illumination wavelength peak at 515 nm (325 $mW \cdot cm^{-2}$), the other one with the illumination peak at 465 nm (750 $mW \cdot cm^{-2}$). After filling 60 μl colorimetric urea solution (equivalent concentration: 0, 1, 5, 10, 25, 50 mM) in the solution tank of sensing chamber, the photo-detecting cover and LED were placed by following the vertically-integrated sensing scheme as photo-detecting cover (top)/colorimetric sensing chamber (middle)/light source (bottom), as we displayed in Fig. 1(d). The photo-detecting cover was applied for detecting transmitted light intensity varied by the colorimetric urea solutions.

The dynamic urea detection were demonstrated by using respectively the 2 mentioned LEDs (515 nm, 465 nm). The results are shown in **Fig. S6(a) and Fig.**

S6(b). Since each measurement can start to reach a saturated ΔI value in 2 min based on the light-detecting characteristic of Au NPs/IZO PD, we then picked all the ΔI values measured at 2 min for further discussing the calibration relation. Noted that the response current saturating in a few minutes is usually observed in metal oxide based photodetectors **[59-63]**. The response speed is not fast, but is sufficient in colorimetric biosensing. Then, In **Fig. 6(c)**, we plotted the ΔI-equivalent urea concentration relation measured by 515 nm LED as the calibration curve (black curve). Besides, another curve plotted by absorbance-equivalent urea concentration relation (green curve) at 515 nm was also prepared for correlating with the calibration curve. From the green curve, when the equivalent urea concentration increases, the corresponding absorbance at 515 nm rises proportionally. This implies the transmitted light intensity coming from colorimetric sample gradually becomes weaker, and then reacts on the decreased ΔI values found from the black curve. By following the same principle, in **Fig. 6(d)**, the ΔI−equivalent urea concentration relation measured by 465 nm LED as the calibration curve (black curve) was also prepared, and absorbance−equivalent urea concentration relation (blue curve) at 465 nm for making the correlation. On the contrary, from the blue curve, when the equivalent urea concentration increases, the corresponding absorbance at 465 nm gradually decreases. This then oppositely leads to the increased ΔI values as the black curve shows. Based on the calibration curves with opposite variation tendencies respectively prepared by using 515 nm and 465 nm LED for colorimetric urea detection, we not only confirmed the sensing properties, but also verified the wavelength selectivity performed by our vertically-integrated biosensor.

Finally, in order to evaluate the sensitivity for colorimetric urea detection, we further compared the calibration curves respectively measured by 515 nm (green curve) and 465 nm LED (blue curve) in **Fig. 6(e)**. The equivalent urea concentration was presented in log scale for clearly targeting the variation region. Interestingly, from the green curve, it is shown that ΔI for 515 nm LED decreases with concentration increasing from 1-50 mM. The sensitivity reduces in the region of 25-50 mM. In parallel, the blue curve (465 nm LED) shows a sharp increase of sensitivity in the range of 25-50 mM. By carefully combining the 2 calibration curves with their sensitive regions, it's possible to achieve an extended sensing range of our vertically-integrated biosensor from 1 to 50 mM. Such performance is also applicable to screen the risk of CKD for human beings based on salivary urea detection (normal group: 2~6 mM; CKD group: ≥ 10 mM).

4. Conclusion

In this work, a compact biosensor for colorimetric sensing with total thickness less than 5 mm has been proposed by integrating a NIR laser-annealed Au NPs/IZO PD fabricated on resin cover with a 3D-printed sensing chamber. In order to obtain good photoresponsivity of PD without damaging the resin substrate, the NIR laser annealing process with 2 main Stages were carefully investigated for both the formation of disconnected Au NPs (Stage A) and the thermoplasmonic-enhanced curing of sol-gel IZO (Stage B). With the use of thermal imager for monitoring the temperature profile, the proper conditions for Au NPs synthesis on molded resin substrates (Substrate-I) were firstly characterized, the photo-induced thermoplasmonic effect was then confirmed for dominating sol-gel IZO curing. The UV-vis photoresponse was improved by increasing the Stage B laser power intensity (16.4

$W \cdot cm^{-2}$) with shorter irradiation time (3 min) in order to keep the maximum temperature at 250 °C.

Then, the NIR laser annealing was applied for PD fabrication on two-kinds of 3D-printed substrates, one with the pristine rough surface (Substrate-II) and the other one with a smoothened surface (Substrate-III). Since only the PDs fabricated on Substrate-III could perform the good photoresponsivity as those on the molded Substrate-I, revealing that the surface planarization is critical. Moreover, increasing IZO thickness can further improve the photoresponsivity with improved homogeneity of Au NPs/IZO nanocomposite film. The optimized sample delivers good-enough UV-vis photoresponsivity (5.9×10^{-1} A/W for 410 nm, 5.2×10^{-3} A/W for 465 nm, 1.4×10^{-3} A/W for 515 nm, and 2.0×10^{-4} A/W for 630 nm) with long operation lifetime ($\geq$1 month). Comparing to traditional thermal annealing process, NIR laser annealing can promote sol-gel IZO curing at low surface temperatures (200~270 °C) within shorter processing time ($\leq$10 min).

Finally, by embedding the optimized NIR laser-annealed Au NPs/IZO PD, the integrated-biosensor was able to demonstrate colorimetric urea sensing with equivalent concentration varied from 1, 5, 10, 25, 50 mM in only 2 min. Double wavelength calibration curves were also established to allow large sensing dynamic range. Such performance may be applicable for screening chronic kidney disease based on the salivary urea detection. We're also expecting that by further applying printing coating technics for fabricating the NIR laser annealed-Au NPs/IZO PD, the photo-induced thermoplasmonic effects can still efficiently assist the PD fabrication on functional 3D-printed designs for extended colorimetric sensing applications.

Acknowledgement

The authors would like to acknowledge the support of Institute and Ministry of Science and Technology (MOST), Taiwan (Project MOST 109-2221-E-009-156-MY2, MOST 110-2221-E-A49-008- and MOST 108-2923-E-009-002-MY3) and the Higher Education Sprout Project of the National Yang Ming Chiao Tung University and Ministry of Education (MOE), Taiwan, Agence Nationale pour la recherche (Project ANR-18-CE24-0028), Région Grand-Est and Institut Carnot MICA. This work of the Interdisciplinary Institute HiFunMat, as part of the ITI 2021-2028 program of the University of Strasbourg, CNRS and Inserm, was supported by IdEx Unistra (ANR-10-IDEX-0002) and SFRI (STRAT'US project, ANR-20-SFRI-0012) under the framework of the French Investments for the Future Program. We also gratefully thank Ludovic Josien for the technical assistance.

References:

[1] M. M. Dhanvijay & S. C. Patil, Internet of Things: A survey of enabling technologies in healthcare and its applications, Computer Networks, 153, 113-131, (2019)

[2] V. Jagadeeswari, V. Subramaniyaswamy, R. Logesh & V. Vijayakumar, A study on medical Internet of Things and Big Data in personalized healthcare system, Health information science and systems, 6(1), 1-20, (2018)

[3] E. K. Naeini, I. Azimi, A. M. Rahmani, P. Liljeberg & N. Dutt, A real-time PPG quality assessment approach for healthcare Internet-of-Things, Procedia Computer Science, 151, 551-558, (2019)

[4] Z. Yan, H. Yuan, Q. Zhao, L. Xing, X. Zheng, W. Wang, Y. Zhao, Y. Yu, L. Hu & W. Yao, Recent developments of nanoenzyme-based colorimetric sensors for heavy metal detection and the interaction mechanism, Analyst, 145(9), 3173-3187, (2020)

[5] B. Yu, F. Zhai, H. Cong & D. Yang, Photosensitive polystyrene/silver bromide hybrid colloidal crystals as recoverable colorimetric naked eye probes for bromine gas sensing, Journal of Materials Chemistry C, 4(7), 1386-1391, (2016)

[6] J. Zeng, M. Li, A. Liu, F. Feng, T. Zeng, W. Duan, M. Li, M. Gong, C. Y. Wen & Y. Yin, Au/AgI dimeric nanoparticles for highly selective and sensitive colorimetric detection of hydrogen sulfide, Advanced Functional Materials, 28(26), 1800515, (2018)

[7] P. T. Trieu & N. Y. Lee, Paper-based all-in-one origami microdevice for nucleic acid amplification testing for rapid colorimetric identification of live cells for

point-of-care testing, Analytical chemistry, 91(17), 11013-11022, (2019)

[8] V. K. Singh, P. K. Yadav, S. Chandra, D. Bano, M. Talat & S. H. Hasan, Peroxidase mimetic activity of fluorescent NS-carbon quantum dots and their application in colorimetric detection of H_2O_2 and glutathione in human blood serum, Journal of Materials Chemistry B, 6(32), 5256-5268, (2018)

[9] L. Hu, H. Liao, L. Feng, M. Wang & W. Fu, Accelerating the peroxidase-like activity of gold nanoclusters at neutral pH for colorimetric detection of heparin and heparinase activity, Analytical chemistry, 90(10), 6247-6252, (2018)

[10] B. Liu, J. Zhuang & G. Wei, Recent advances in the design of colorimetric sensors for environmental monitoring, Environmental Science: Nano, 7(8), 2195-2213, (2020)

[11] G. Alberti, C. Zanoni, L. R. Magnaghi & R. Biesuz, Disposable and low-cost colorimetric sensors for environmental analysis, International Journal of Environmental Research and Public Health, 17(22), 8331, (2020)

[12] Y. Guo, C. Liu, R. Ye & Q. Duan, Advances on water quality detection by UV-vis spectroscopy, Applied Sciences, 10(19), 6874, (2020)

[13] Ö. Kap, V. Kılıç, J. G. Hardy & N. Horzum, Smartphone-based colorimetric detection systems for glucose monitoring in the diagnosis and management of diabetes, Analyst, 146(9), 2784-2806, (2021)

[14] Y. Xing, Q. Zhu, X. Zhou & P. Qi, A dual-functional smartphone-based sensor for colorimetric and chemiluminescent detection: A case study for fluoride concentration mapping, Sensors and Actuators B: Chemical, 319, 128254, (2020)

[15] L. Kong, Y. Gan, T. Liang, L. Zhong, Y. Pan, D. Kirsanov, A. Legin, H. Wan & P. Wang, A novel smartphone-based CD-spectrometer for high sensitive and cost-effective colorimetric detection of ascorbic acid, Analytica Chimica Acta,

1093, 150-159, (2020)

[16] A. Amirjani & D. H. Fatmehsari, Colorimetric detection of ammonia using smartphones based on localized surface plasmon resonance of silver nanoparticles, Talanta, 176, 242-246, (2018)

[17] L. Zheng, P. Qi & D. Zhang, A simple, rapid and cost-effective colorimetric assay based on the 4-mercaptophenylboronic acid functionalized silver nanoparticles for bacteria monitoring, Sensors and Actuators B: Chemical, 260, 983-989, (2018)

[18] F. Liu, R. Chen, W. Song, L. Li, C. Lei & Z. Nie, Modular combination of proteolysis-responsive transcription and spherical nucleic acids for smartphone-based colorimetric detection of protease biomarkers, Analytical Chemistry, 93(7), 3517-3525, (2021)

[19] Y. Fan, J. Li, Y. Guo, L. Xie & G. Zhang, Digital image colorimetry on smartphone for chemical analysis: A review, Measurement, 171, 108829, (2021)

[20] B. S. Boruah & R. Biswas, An optical fiber based surface plasmon resonance technique for sensing of lead ions: A toxic water pollutant, Optical Fiber Technology, 46, 152-156, (2018)

[21] M. Malekovic, M. Urann, U. Steiner, B. D. Wilts & M. Kolle, Soft photonic fibers for colorimetric solvent vapor sensing, Advanced Optical Materials, 8(13), 2000165, (2020)

[22] N. H. M. Yusoff, L. R. I. Teo, S. J. Phang, V. L. Wong, K. H. Cheah & S. S. Lim, Recent advances in polymer-based 3D printing for wastewater treatment application: an overview, Chemical Engineering Journal, 429, 132311, (2022)

[23] K. Kadimisetty, J. Song, A. M. Doto, Y. Hwang, J. Peng, M. G. Mauk, F. D. Bushman, R. Gross, J. N. Jarvis & C. Liu, Fully 3D printed integrated reactor

array for point-of-care molecular diagnostics, Biosensors and Bioelectronics, 109, 156-163, (2018)

[24] K. Yin, X. Ding, Z. Xu, Z. Li, X. Wang, H. Zhao, C. Otis, B. Li & C. Liu, Multiplexed colorimetric detection of SARS-CoV-2 and other pathogens in wastewater on a 3D printed integrated microfluidic chip, Sensors and Actuators B: Chemical, 344, 130242, (2021)

[25] H. N. Chan, Y. Shu, B. Xiong, Y. Chen, Y. Chen, Q. Tian, S. A. Michael, B. Shen & H. Wu, Simple, cost-effective 3D printed microfluidic components for disposable, point-of-care colorimetric analysis, ACS Sensors, 1(3), 227-234, (2016)

[26] S. H. Baek, C. Park, J. Jeon & S. Park, Three-dimensional paper-based microfluidic analysis device for simultaneous detection of multiple biomarkers with a smartphone, Biosensors, 10(11), 187, (2020)

[27] G. Wang, Z. Cai & X. Dou, Colorimetric logic design for rapid and precise discrimination of nitrate-based improvised explosives, Cell Reports Physical Science, 2(2), 100317, (2021)

[28] Y. Liang, Q. Liu, S. Liu, X. Li, Y. Li & M. Zhang, One-step 3D printed flow cells using single transparent material for flow injection spectrophotometry. Talanta, 201, 460-464, (2019)

[29] C. J. Moon & H. S. Kim, Intense pulsed light annealing process of indium–gallium–zinc–oxide semiconductors via flash white light combined with deep-UV and near-infrared drying for high-performance thin-film transistors, ACS applied materials & interfaces, 11(14), 13380-13388, (2019)

[30] N. Tiwari, A. Nirmal, M. R. Kulkarni, R. A. John & N. Mathews. Enabling high performance n-type metal oxide semiconductors at low temperatures for thin film

transistors, Inorganic Chemistry Frontiers, 7(9), 1822-1844, (2020)

[31] A. Mancinelli, S. Bolat, J. Kim, Y. E. Romanyuk & D. Briand, Deep-UV-Enhanced Approach for Low-Temperature Solution Processing of IZO Transistors with High-k $AlO_x/YAlO_x$ Dielectric, ACS Applied Electronic Materials, 2(10), 3141-3151, (2020)

[32] Y. H. Kim, J. S. Heo, T. H. Kim, S. Park, M. H. Yoon, J. Kim, M. S. Oh, G. R. Yi, Y. Y. Noh & S. K. Park, Flexible metal-oxide devices made by room-temperature photochemical activation of sol–gel films, Nature, 489(7414), 128-132, (2012)

[33] H. C. Lin, F. Stehlin, O. Soppera, H. W. Zan, C. H. Li, F. Wieder, A. Ponche, D. Berling, B. H. Yeh, K. H. Wang, Deep ultraviolet laser direct write for patterning sol-gel InGaZnO semiconducting micro/nanowires and improving field-effect mobility, Scientific reports, 5(1), 1-11, (2015)

[34] C. C. Yeh, H. C. Liu, M. Y. Chuang, J. Denzer, D. Berling, H. W. Zan, O. Soppera, Controllable formation of zinc oxide micro-and nanostructures via DUV direct patterning, Advanced Materials Interfaces, 3(19), 1600373, (2016)

[35] C. C. Yeh, S. Colis, P. Fioux, H. W. Zan, D. Berling, O. Soppera, Nanoscale ferromagnetic cobalt-doped ZnO structures formed by deep-UV direct-patterning, Advanced Materials Interfaces, 4(22), 1700738, (2017)

[36] J. Shao, C. Ruan, H. Xie, Z. Li, H. Wang, P. K. Chu & X. F. Yu, Black-phosphorus-incorporated hydrogel as a sprayable and biodegradable photothermal platform for postsurgical treatment of cancer, Advanced Science, 5(5), 1700848, (2018)

[37] X. Zhang, Y. L. Chen, R. S. Liu & D. P. Tsai, Plasmonic photocatalysis, Reports on Progress in Physics, 76(4), 046401, (2013)

[38] C. F. Lin, A. Khitous, H. W. Zan & O. Soppera, Exploiting thermoplasmonic effects for laser-assisted preparation of Au nanoparticles/InZnO thin film with visible range photodetection properties, Advanced Optical Materials, 9(22), 2100045, (2021)

[39] Z. Zhang, C. Zhang, H. Zheng & H. Xu, Plasmon-driven catalysis on molecules and nanomaterials, Accounts of Chemical Research, 52(9), 2506-2515, (2019)

[40] E. Z. Bilbilova, A. S. Ivkovska & V. Ambarkova, Correlation between salivary urea level and dental caries, Prilozi, 33(1), 289-302, (2012)

[41] G. Suresh, A. R. Kiran, Y. Samata, N. P. Naik & A. V. Kumar, Analysis of blood and salivary urea levels in patients undergoing haemodialysis and kidney transplant, Journal of clinical and diagnostic research: JCDR, 8(7), ZC18, (2014)

[42] T. J. Lasisi, Y. R. Raji & B. L. Salako, Salivary creatinine and urea analysis in patients with chronic kidney disease: a case control study, BMC nephrology, 17(1), 1-6, (2016)

[43] A. Stiles, W. Kobler, P. Yeole & U. Vaidya, Photopolymer formulation towards large scale additive manufacturing of autoclave capable tooling, Additive Manufacturing, 102571, (2021)

[44] W. Xie, L. Lei, M. Tian, Z. Zhang & Y. Liu, A high-resolution colorimetric immunoassay platform realized by coupling enzymatic multicolor generation with smartphone readout, Analyst, 143(12), 2901-2907, (2018)

[45] F. Ruffino, A. Pugliara, E. Carria, C. Bongiorno, C. Spinella & M. G. Grimaldi, Formation of nanoparticles from laser irradiated Au thin film on SiO_2/Si: Elucidating the Rayleigh-instability role, Materials Letters, 84, 27-30, (2012)

[46] Y. Oh, J. Lee & M. Lee, Fabrication of Ag-Au bimetallic nanoparticles by laser-induced dewetting of bilayer films, Applied Surface Science, 434, 1293-1299,

(2018)

[47] S. C. Park, D. Kim, H. Shin, D. K. Lee, X. Zhang, J. Park & J. S. Choi, Advanced photo-annealing of indium zinc oxide films for thin-film transistors using pulse UV light, Journal of Information Display, 17(1), 1-7, (2016)

[48] P. Pattanasattayavong, S. Rossbauer, S. Thomas, J. G. Labram, H. J. Snaith & T. D. Anthopoulos, Solution-processed dye-sensitized ZnO phototransistors with extremely high photoresponsivity, Journal of Applied Physics, 112(7), 074507, (2012)

[49] M. Sbeta, A. Atilgan, A. Atli & A. Yildiz, Influence of the spin acceleration time on the properties of ZnO:Ga thin films deposited by sol–gel method, Journal of Sol-Gel Science and Technology, 86(2), 513-520, (2018)

[50] T. Leng, K. Parvez, K. Pan, J. Ali, D. McManus, K. S. Novoselov, C. Casiraghi & Z. Hu, Printed graphene/WS_2 battery-free wireless photosensor on papers, 2D Materials, 7(2), 024004, (2020)

[51] V. T. Tran, Y. Wei & H. Du, On-substrate joule effect heating by printed micro-heater for the preparation of ZnO semiconductor thin film, Micromachines, 11(5), 490, (2020)

[52] V. T. Tran, Y. Wei, H. Yang, Z. Zhan & H. Du, All-inkjet-printed flexible ZnO micro photodetector for a wearable UV monitoring device, Nanotechnology, 28(9), 095204, (2017)

[53] R. F. Hossain, I. G. Deaguero, T. Boland & A. B. Kaul, Biocompatible, large-format, inkjet printed heterostructure MoS_2-graphene photodetectors on conformable substrates, npj 2D Materials and Applications, 1(1), 1-10, (2017)

[54] M. Min, R. F. Hossain, N. Adhikari & A. B. Kaul, Inkjet-printed organohalide 2D layered perovskites for high-speed photodetectors on flexible polyimide

substrates, ACS applied materials & interfaces, 12(9), 10809-10819, (2020)

[55] S. H. Park, R. Su, J. Jeong, S. Z. Guo, K. Qiu, D. Joung, F. Meng & M. C. McAlpine, 3D printed polymer photodetectors, Advanced Materials, 30(40), 1803980, (2018)

[56] X. Shan, P. Mao, H. Li, T. Geske, D. Bahadur, Y. Xin, S. Ramakrishnan & Yu, Z, 3D-printed photoactive semiconducting nanowire–polymer composites for light sensors, ACS Applied Nano Materials, 3(2), 969-976, (2019)

[57] D. Lee, M. L. Seol, G. Motilal, B. Kim, D. I. Moon, J. W. Han & M. Meyyappan, All 3D-printed flexible ZnO UV photodetector on an ultraflat substrate, ACS sensors, 5(4), 1028-1032, (2020)

[58] L. Li, Z. Lou, H. Chen, R. Shi & G. Shen, Stretchable SnO_2-CdS interlaced-nanowire film ultraviolet photodetectors, Sci China Mater, 62, 1139-1150, (2019)

[59] N. Kumar, K. Arora & M. Kumar, Role of oxygen and boron to control the duality behavior and thermal stability in Boron doped amorphous indium-zinc-oxide thin films, Semiconductor Science and Technology, 34(5), 055004, (2019)

[60] S. J. Chang, B. G. Duan, C. H. Hsiao, S. J. Young, B. C. Wang, T. H. Kao, K. S. Tsai & S. L. Wu, Low-frequency noise characteristics of in-doped ZnO ultraviolet photodetectors, IEEE Photonics Technology Letters, 25(21), 2043-2046, (2013)

[61] D. Kim, E. Jo & J. Y. Leem, Thermal dissipation annealing for crystallization of In-doped ZnO films deposited on polyethylene naphthalate substrate without substrate deformation, physica status solidi (a), 218(16), 2000698. (2021)

[62] A. Kushwaha & M. Aslam, Defect induced high photocurrent in solution grown vertically aligned ZnO nanowire array films, Journal of Applied Physics, 112(5),

054316, (2012)

[63] X. Wang, K. Liu, X. Chen, B. Li, M. Jiang, Z. Zhang, H. Zhao & D. Shen,. Highly wavelength-selective enhancement of responsivity in Ag nanoparticle-modified ZnO UV photodetector, ACS applied materials & interfaces, 9(6), 5574-5579, (2017)

Supporting information:

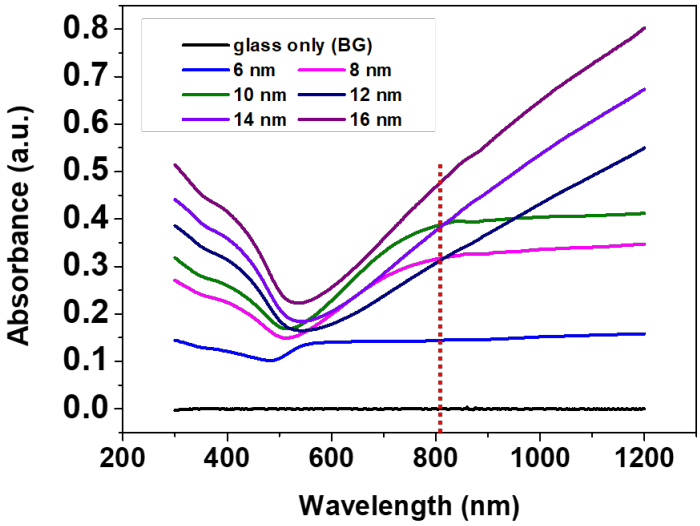

Fig. S1: The absorption spectra of Au film thickness deposited on glass substrate with the variation from 6 nm to 16 nm

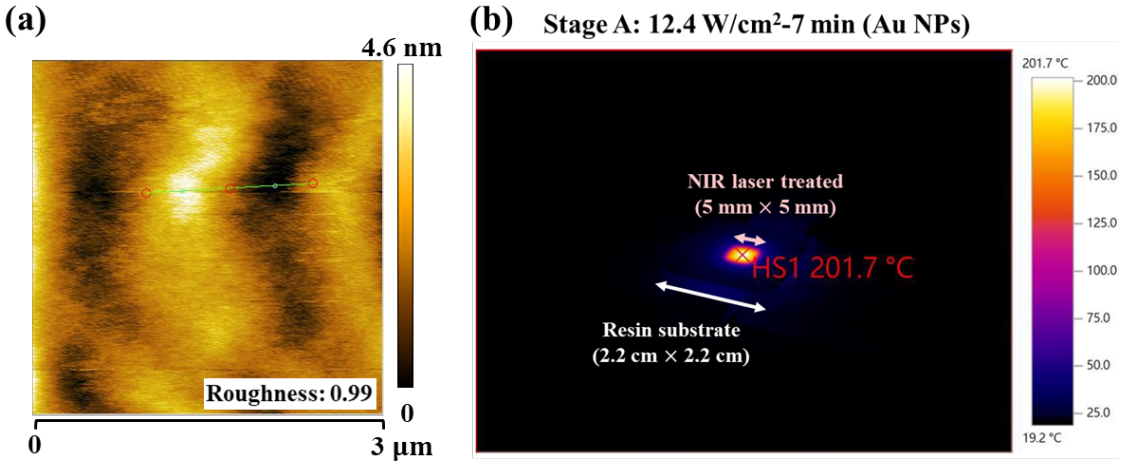

Fig. S2: (a) The surface morphology of Substrate-I; (b) the surface temperature profile analyzed by the thermal imager for the Au NPs formed from 6-nm-thick Au film by Stage A annealing (12.4 W·cm^{-2}-7 min) on Substrate-I

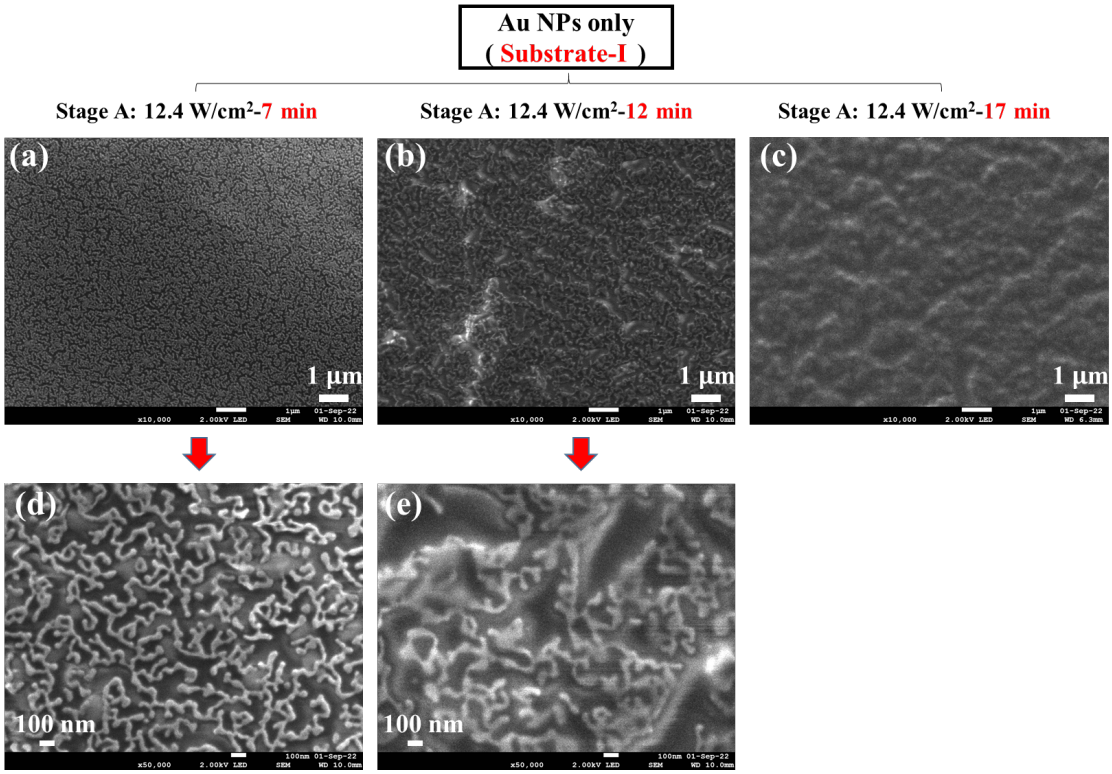

Fig. S3: The SEM analysis of NIR laser-annealed Au NPs formed by Stage A: 12.4 W·cm^{-2} with processing time as (a) 7 min, (b) 12 min and (c) 17 min on Substrate-I (×10000 magnification). Also, the images with higher magnification rate (×50000) of Fig. S3(a) and Fig. S3(b) are respectively shown in Fig. S3(d) and Fig. S3(e).

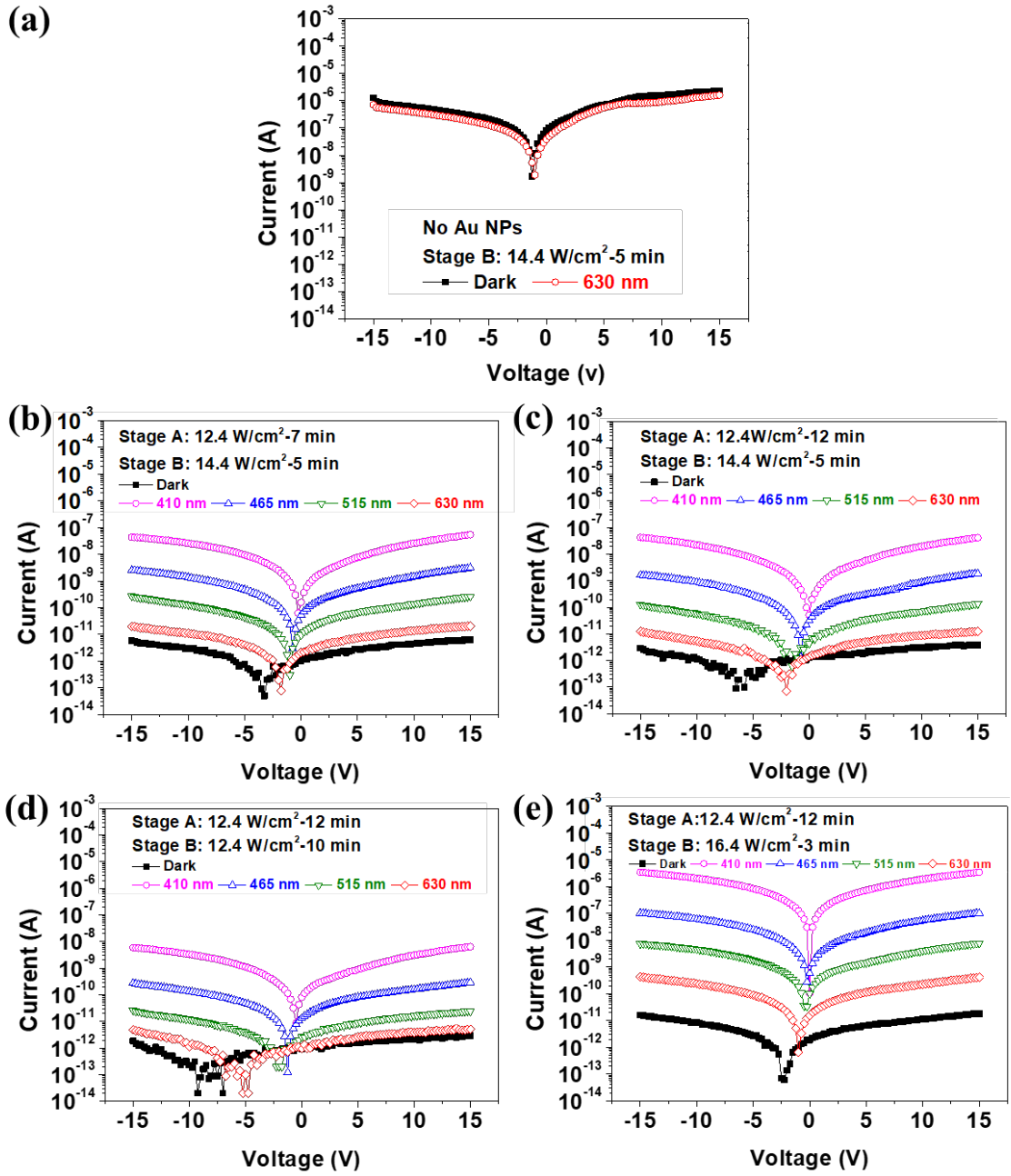

Fig. S4: The UV-vis light/dark current performance of Au NPs/IZO PDs on Substrate-I with NIR laser annealing conditions as (a) No Au NPs/IZO (14.4 W·cm^{-2}-5 min) (b) Au NPs (12.4 W·cm^{-2}-7 min)/IZO (14.4 W·cm^{-2}-5 min) (c) Au NPs (12.4 W·cm^{-2}-12 min)/IZO (14.4 W·cm^{-2}-5 min) (d) Au NPs (12.4 W·cm^{-2}-12 min)/IZO (12.4 W·cm^{-2}-10 min) (e) Au NPs (12.4 W·cm^{-2}-12 min)/IZO (16.4 W·cm^{-2}-3 min); all with IZO coating: 2000 rpm-50 sec

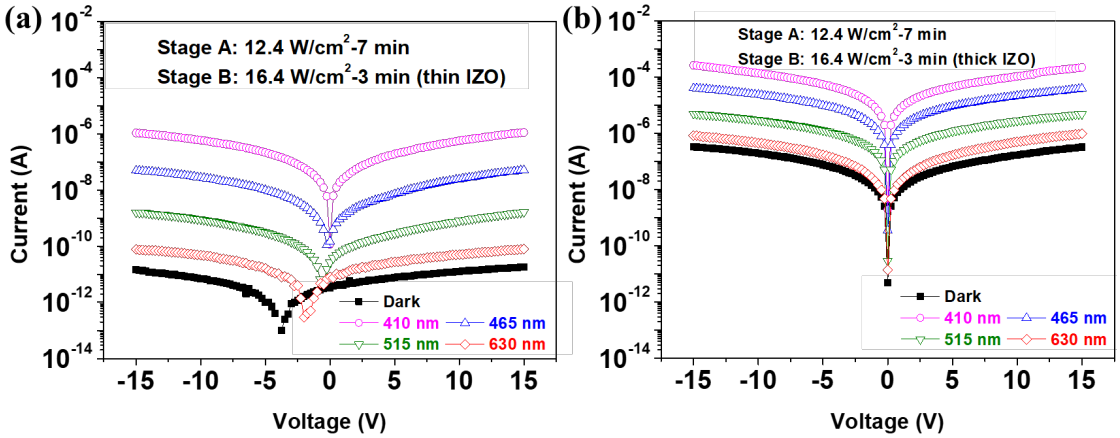

Fig. S5: The UV-vis light/dark current performance of NIR laser annealed Au NPs/IZO PDs ((Stage A: 12.4 W·cm^{-2}-7 min), (Stage B: 16.4 W·cm^{-2}-3 min)) fabricated on Substrate-III with sol-gel IZO solution coating condition as (a) 2000 rpm-50 sec (thin) (b) 700 rpm-60 sec (thick).

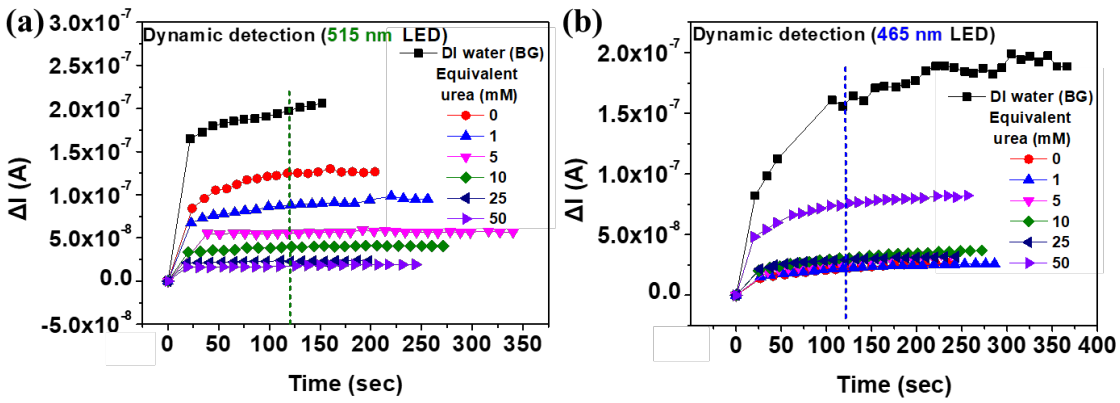

Fig. S6: The dynamic detection of miniaturized biosensor for colorimetric urea detection measured with (a) 515 nm (b) 465 nm LED